### Phase field modeling of domain dynamics and polarization accumulation in ferroelectric HZO

Cite as: Appl. Phys. Lett. 114, 202903 (2019); https://doi.org/10.1063/1.5092707 Submitted: 13 February 2019 . Accepted: 04 May 2019 . Published Online: 23 May 2019

Atanu K. Saha, Kai Ni, Sourav Dutta, Suman Datta, and Sumeet Gupta 🔟







#### ARTICLES YOU MAY BE INTERESTED IN

Piezoelectricity and electrostriction in ferroelastic materials with polar twin boundaries and domain junctions

Applied Physics Letters 114, 202901 (2019); https://doi.org/10.1063/1.5092523

Oxygen vacancy mediated conductivity and charge transport properties of epitaxial Ba<sub>0.6</sub>La<sub>0.4</sub>TiO<sub>3- $\delta$ </sub> thin films

Applied Physics Letters 114, 202902 (2019); https://doi.org/10.1063/1.5093749

Field-dependent charging phenomenon of HVDC spacers based on dominant charge behaviors

Applied Physics Letters 114, 202904 (2019); https://doi.org/10.1063/1.5096228





# Phase field modeling of domain dynamics and polarization accumulation in ferroelectric HZO

Cite as: Appl. Phys. Lett. **114**, 202903 (2019); doi: 10.1063/1.5092707 Submitted: 13 February 2019 · Accepted: 4 May 2019 · Published Online: 23 May 2019







Atanu K. Saha, 1,a) Kai Ni, 2 Sourav Dutta, 2 Suman Datta, 2 and Sumeet Gupta 1

#### **AFFILIATIONS**

- <sup>1</sup>School of Electrical and Computer Engineering, Purdue University, West Lafayette, Indiana 47907, USA
- <sup>2</sup>Department of Electrical Engineering, University of Notre Dame, Notre Dame, Indiana 46556, USA

#### **ABSTRACT**

In this work, we investigate the accumulative polarization (P) switching characteristics in ferroelectric (FE) thin films under the influence of sequential sub-coercive electric-field pulses. Performing the dynamic phase-field simulation (based on time-dependent Landau-Ginzburg model) and experimental measurement on  $Hf_{0.4}Zr_{0.6}O_2$  (HZO), we analyze the electric field induced domain-wall (DW) motion and the resultant P accumulation process in FE. According to our analysis, even in the absence of an applied electric field, the DW can potentially undergo spontaneous motion. Such a DW instability leads to *spontaneous* P-excitation and relaxation processes, which play a pivotal role in accumulative P-switching in an FE grain. We show that the extent of such P accumulation increases with the increase in the applied electric field, increase in excitation time and decrease in relaxation time. Finally, by considering an ensemble of grains with local and global coercive field distributions, we model the P-accumulation process in a large area HZO sample. In such a multi-grain scenario, the dependency of P accumulation on the applied electric field pulse attributes follows similar features as that of a single-grain, although the spontaneous processes (excitation/relaxation) are less prominent in large area sample.

Published under license by AIP Publishing. https://doi.org/10.1063/1.5092707

Ferroelectric (FE) materials, particularly Zr doped HfO<sub>2</sub> (Hf<sub>1-x</sub>Zr<sub>x</sub>O<sub>2</sub>:HZO<sup>1</sup>), have drawn significant research interest in recent times due to CMOS process compatibility,<sup>2</sup> thickness scalability,<sup>2</sup> and many promising attributes of ferroelectric field effect transistors<sup>2</sup> (FEFETs) for multiple applications.<sup>2-4</sup> Furthermore, a newly reported accumulative polarization (*P*)-switching process<sup>5</sup> in FE leads to many appealing opportunities for novel applications<sup>6</sup> and computing.<sup>7</sup> For such emerging applications of FEFETs, the *P*-switching dynamics in response to sub/super-coercive voltage pulse trains play an important role and are, therefore, critical to understand.

To that effect, this letter analyzes spatially local P-switching dynamics and its participation in globally observable P-accumulation characteristics in response to a voltage pulse train. Our analysis is based on a dynamic phase field model  $^{8,9}$  coupled with measured accumulation characteristics of HZO. By providing the spatial distribution of P (P-map) in different electric field (E-field) excitation and relaxation steps, we discuss different types of P excitation and relaxation processes and their corresponding dependency on E-field (E) amplitude ( $E^{app}_{max}$ ), ON time (or excitation time  $T_{on}$ ), and OFF time of the pulse (or relaxation time  $T_{off}$ ). Finally, considering a coercive-field distribution among different FE grains, we analyze the overall P-accumulation characteristics.

Let us start by describing the experimentally observed trends in P-switching characteristics in HZO. Figure 1(a) shows the measured charge vs E-field (Q–E) characteristics of a 10 nm HZO film [x = 0.6, grown by atomic layer deposition (ALD) with the tungsten (W) capping layer as top and bottom contacts]. Here,  $Q = P + \epsilon_0 E$ , where  $\epsilon_0$  is the vacuum permittivity. We observe accumulative P-switching in HZO as the response of successive E-field stimulation [Fig. 1(b)], where the P-accumulation ( $P^{acc}$ ) characteristics exhibit a strong dependence on the E-pulse properties. For example, we observe faster  $P^{acc}$ with the increase in  $E_{max}^{app}$  [Fig. 1(c)], increase in  $T_{on}$  [Fig. 1(d)], and/or decrease in  $T_{off}$  [Fig. 1(e)]. Also,  $P^{acc}$  saturates after a certain number of pulses. Such saturation occurs at higher P with the increase in  $E_{max}^{app}$ , increase in  $T_{on}$ , and decrease in  $T_{off}$ . It is noteworthy that such accumulated-P observed in the experiments is the average of locally accumulated-P in different grains. 10 Hence, to explain the experimental results described above, it is critical to understand the spatially local Pswitching dynamics in an individual grain. We analyze such processes in detail based on our phase-field model, calibrated to the experiments. Note that several sophisticated 2D/3D phase-field models have been developed for multiaxial ferroelectrics. However, in this paper, our motivation is not to develop such a comprehensive model for HZO, but to establish a physical understanding of the underlying

a) Electronic mail: saha26@purdue.edu.

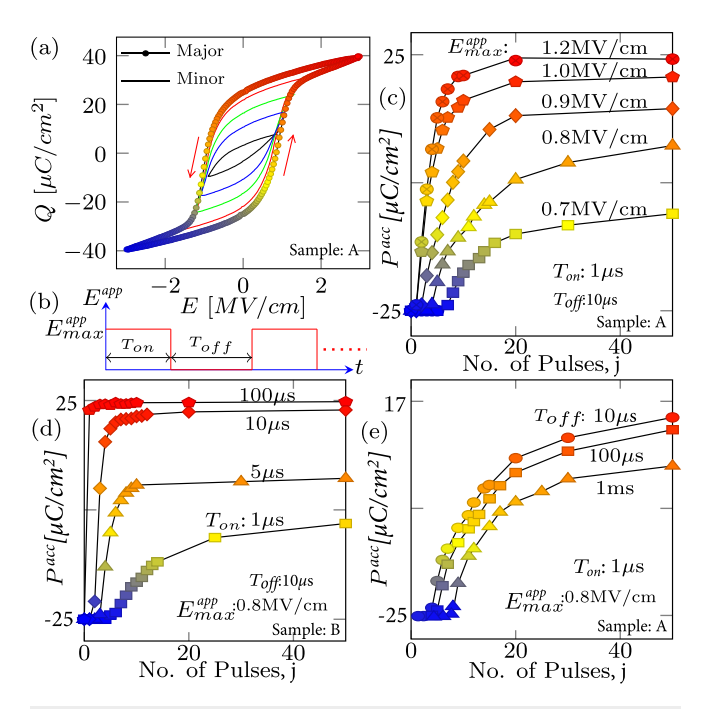


**FIG. 1.** (a) Q-E curves of a 10 nm HZO film. (b) Applied E-field pulses showing pulse-amplitude  $(E_{max}^{app})$ , excitation time  $(T_{on})$ , and relaxation time  $(T_{off})$ . Accumulated polarization  $(P^{acc})$  vs number of E-field pulses (j) for different (c)  $E_{max}^{app}$ , (d)  $T_{on}$ , and (e)  $T_{off}$ . Here, the results shown in (a), (c), and (e) are measured on the same HZO sample (sample: A) and the results shown in (d) are measured on a different HZO sample (sample: B).

mechanism of accumulative polarization switching based on a simplified approach.  $^{14,15}$ 

According to recent studies, <sup>16,17</sup> the origin of ferroelectricity in HZO has been regarded as the stability of the polar orthorhombic (o) phase, where the polarization (P) direction is along the c-axis of the ophase. <sup>16,17</sup> In our model, we assume that the c-axis is parallel to the film thickness direction (z-axis). This implies that the P direction is only along the thickness (z-axis). Hence,  $P_x = 0$ ,  $P_y = 0$ , and  $P_z \neq 0$ .  $P_z$  can have a spatial distribution in the x-y plane. However, we assume uniform  $P_z$  along the z-axis ( $dP_z/dz = 0$ ) owing to the ultrathin nature of the film ( $\sim$ 10 nm). The time-dependent and spatial evolution of polarization switching can be described by the time (t)-dependent Landau-Ginzburg (TDLG) equation: <sup>9,18</sup>  $\delta F/\delta P_z = -\rho(\partial P_z/\partial t)$ . Here,  $\rho$  is the kinetic coefficient and F is the total energy of the system. Considering up to the 6th order terms in Landau's free energy expansion, <sup>19</sup> the normalized representation of the TDLG equation within the FE is given by the following equation: <sup>14,15</sup>

$$-\rho_n \frac{\partial P_n}{\partial t} = -K_p^n \nabla^2 P_n - E_n^{app} + \hat{\alpha} P_n + \hat{\beta} P_n^3 + \hat{\gamma} P_n^5. \tag{1}$$

Here,  $P_n (= P_z/P_{CO})$  and  $E_n^{app} (= E^{app}/E_{CO})$  are the polarization and applied E-field normalized with respect to  $E_{CO}$  (coercive field of a non-interacting lattice, E at dP/dE=0) and  $P_{CO}$  (P at  $E=E_{CO}$ ), respectively. Note that the normalized coercive field = 1.  $\hat{\alpha}$ ,  $\hat{\beta}$ , and  $\hat{\gamma}$  are the normalized effective Landau coefficients,  $\frac{14,20,21}{2}$  and the calibrated values are -1.499, +0.498, and 0.001, respectively. Also,  $\rho_n$  is the normalized

kinetic coefficient and  $K_p^n$  is the normalized domain-interaction parameter (equivalent to the gradient energy coefficient). In our simulations, we self-consistently solve Eq. (1) in a real space grid ( $\Delta x = 0.25 \, \mathrm{nm}$  and  $\Delta y = 0.25 \, \mathrm{nm}$ ) by considering the Neumann boundary at the edges. We include a comprehensive discussion on parameter extraction, normalization, and simulation methodology in the supplementary material. It is noteworthy that  $P_n$  denotes normalized microscopic P in each grid point, while the analogous quantity of experimentally measured P is the spatial average of  $P_m$  denoted as  $\bar{P}_n$ . Also,  $K_p^n \nabla^2 P_n$  can be thought of as the local effective interaction Efield,  $E_n^{int}$ . Therefore, the P-switching depends on  $E_n^{app} + E_n^{int}$ . For instance, P-switching will occur for  $|E_n^{app} + E_n^{int}| > 1$  (since the normalized coercive field = 1).

In general, P-switching can take place in two different ways, namely, (i) direct nucleation and (ii) domain-wall (DW) assisted nucleation. To understand these processes, let us start by considering the FE sample in Fig. 2(a), where region R1 exhibits  $P_n = +|P_{n,r}|$  and R2 exhibits  $P_n = -|P_{n,r}|$  and they are separated by a DW within which  $P_n$  varies gradually along the x-axis [Fig. 2(b)]. Here,  $P_{n,r}$  is the remanent polarization. In this case, the domain structure is effectively 1D as  $d^2P_n/dy^2 = 0$ . Note that the considered width (along y-axis) of the grain is lower than a DW width ( $\sim 3$  nm, for  $K_p^n = 1$ ), and therefore, a DW formation will not occur in the y-axis direction. Now, direct nucleation occurs for super-coercive applied fields ( $|E_n^{app}| > 1$ ), wherein region R2 will switch to +P at once if the E-field is applied for a sufficient time. On the other hand, DW assisted nucleation (which is the main focus of this work) is observed for subcoercive applied fields  $(|E_n^{app}| < 1)$ , in which  $E_n^{int}$  plays a key role. To explain this, let us consider  $E_n^{app} = 0$  and static condition  $(dP_n/dt = 0)$ . Hence, Eq. (1) can be written as  $E_n^{int} = K_p^n \nabla^2 P_n = \hat{\alpha} P_n + \hat{\beta} P_n^3 + \hat{\gamma} P_n^5$ . Note that  $E_n^{int}$  is localized and nonzero only within DW [Fig. 2(c)] (except the DW center, at the DW center  $E_n^{int} = 0$ ). Figure 2(d) shows the relation between  $E_n^{int}$  and  $P_n$ , signifying that the symmetric spatial distribution of  $P_n$ provides a symmetric  $E_n^{int}$  for a 1D DW. Here, the symmetric  $E_n^{int}$ yields a stable and static DW for  $E_n^{app} = 0$  by balancing the forces due to  $E_n^{int}$  ( $\propto PE_n^{int}$ ) on the two sides of the DW. This can also be understood by noting that  $|E_n^{int}| \leq 1$ , which leads to stable DW due to no Pswitching in the absence of an applied E-field. However, by applying a

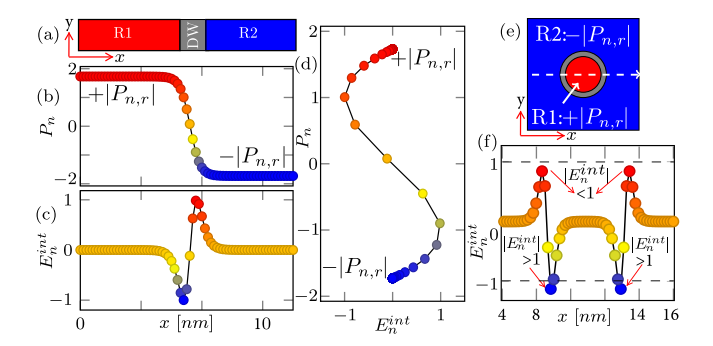


**FIG. 2.** (a) FE structure showing the 1D domain-wall (DW) and spatial distribution of (b) polarization,  $P_n$ , and (c) interaction E-field,  $E_n^{int}$ , that shows symmetric  $E_n^{int}$  distribution in R1 and R2 domains. (d) Static  $P_n$ - $E_n^{int}$  relation. (e) FE structure showing 2D DW and spatial distribution of (f)  $E_n^{int}$  along the *x*-axis showing asymmetric  $E_n^{int}$  distribution in the R1 domain ( $|E_n^{int}| > 1$  at the inner interface) and R2 domain ( $|E_n^{int}| < 1$  at the outer interface).

subcoercive E-field,  $0 < |E_n^{app}| < 1$ , we can get a total local E-field,  $|E_n^{app} + E_n^{int}| > 1$ , and that can eventually initiate *P*-switching. Such *P*-switching is a spatially local and a gradual process with respect to time, which is referred to as DW motion or DW assisted nucleation. (For more details on 1D DW motion-based *P*-switching, see supplementary material.)

With the understanding of the 1D DW, let us now examine 2D DW, for which we analyze two cases by considering a homogeneous coercive field (case-1) and a distribution of a coercive field (case-2) in an FE grain. Let us start with case-1 and consider a square FE sample [Fig. 2(e)] where a circular region R1 exhibits  $P_n = +|P_{n,r}|$ , which is surrounded by R2 with  $P_n = -|P_{n,r}|$ . Here, the DW is 2D, which implies that the degree of freedom of DW motion is "2." In this case,  $\nabla^2 P_n$  in the polar coordinate (assuming an angular independence) can be written as  $\nabla^2 P_n = [(\partial^2 P_n/\partial r^2) + (1/r)(\partial P_n/\partial r)]$ . Now, a radially symmetric polarization distribution  $(P_n(r))$  with a center of symmetry at r = r', both  $\partial^2 P_n / \partial r^2$  and  $\partial P_n / \partial r$  will also be radially symmetric with the same center of symmetry at r = r'. Here, r = r' can be regarded as the center of the DW. However, the 1/r term exhibits a radial symmetry only with respect to r = 0. Therefore,  $\nabla^2 P_n$  becomes radially asymmetric for any arbitrary  $r' \neq 0$ . Consequently,  $E_n^{int}$ becomes spatially asymmetric [Fig. 2(f)], where  $|E_n^{int}| > 1$  at the inner interface and  $|E_n^{int}| < 1$  at the outer interface of DW. Such asymmetry in the  $E_n^{int}$  causes the DW to undergo an effective inward force  $(\propto PE_n^{int})$ . Hence, the DW becomes unstable and the R1 region shrinks spontaneously with time. Such spontaneous phenomena play an important role in the P-switching dynamics that we discuss subsequently. (Note that such a DW instability is in contrast to the 1D case that we discussed above where symmetric  $E_n^{int}$  leads to stable DW).

Let us now consider a sequence of subcoercive E-field pulses  $(E_{n,max}^{app}=E_{max}^{app}/E_{C0}=0.8)$  applied to this sample of FE. Simulated transient  $\bar{P}_n$  is shown in Fig. 3(a) and the initial P-map at t=0 ns is shown in Fig. 3(b-i), where the initially switched region (red) can be assumed as a pinned-type domain. After the arrival of the first E-field pulse, the R1 domain grows circularly, nucleating new lattices sequentially at the outer edge of the DW [Fig. 3(b-ii)]. This implies an increase in the R1 area and a decrease in the R2 area by an amount  $\Delta A_j^+$  (j = E-field pulse number). The corresponding P-excitation characteristics [Fig. 3(a-i-ii)] comprise three different components [Fig. 3(c)], i.e., type-1:  $-|P_{n,r}|$  to  $-|P_{n,e1}|$  (in R2), type-2:  $+|P_{n,r}|$  to  $+|P_{n,e2}|$  (in R1), and type-3:  $-|P_{n,r}|$  to  $+|P_{n,e2}|$  (leads to  $\Delta A_j^+>0$ ).

After the end of the first E-field pulse, the DW propagation stops and the P changes due to type-1 and type-2 excitation components get immediately relaxed to  $-|P_{n,r}|$  and  $+|P_{n,r}|$ , respectively. We call these type-1 and 2 relaxations, respectively [Fig. 3(c)]. Similarly, the newly nucleated area  $(\Delta A_i^+)$  also rapidly get relaxed to  $+|P_{n,r}|$  by following type-2 relaxation. The corresponding transient relaxation in  $\bar{P}_n$  can be seen in Fig. 3(a) [from point ii to ii(a)]. Physically, the type-1 and type-2 excitation/relaxation components can be understood as the applied E-field driven soft dielectric<sup>23</sup> type capacitive charging/discharging event. Interestingly, followed by such rapid relaxation, there is another relaxation component that gradually reduces  $\bar{P}_n$  until the arrival of the next E-field pulse {Fig. 3[a-ii(a)-iii]}. Such spontaneous P-relaxation is the outcome of DW instability (due to  $E_n^{int}$  asymmetry we discussed above) that causes spontaneous shrinking of the R1 domain [Fig. 3(b-ii-iii)]. We define the spontaneous decrease in the R1 area in the absence of the E-field as  $\Delta A_i^-$ .

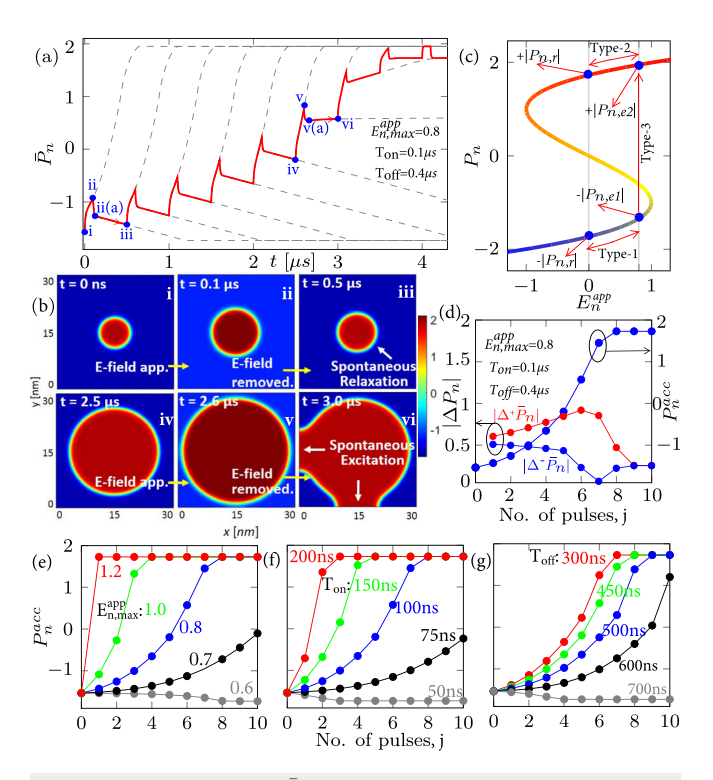


**FIG. 3.** (a) Simulated transient  $\bar{P}_n$  considering case-1 for a sequence of E-field pulses. Corresponding (b) P-map at points i–vi. (c) Static  $P_n$  vs  $E_n^{app}$  showing different stimulated excitation/relaxation components. (d) Increase and decrease in  $P_n$  ( $|\Delta^+\bar{P}_n|$  and  $|\Delta^-\bar{P}_n|$ , respectively) and accumulated P ( $P_n^{acc}$ ) in each excitation/relaxation sequence with respect to the pulse number (j).  $P_n^{acc}$  vs j for different (e)  $E_{n,max}^{app}$ , (f)  $T_{on}$ , and (g)  $T_{off}$ . Here,  $E_{n,max}^{app} = E_{max}^{app}/E_{C0}$ .

Now, due to sequential E-field pulses, the R1 domain grows gradually and the DW moves further toward the grain boundary by following P-excitation (type-1,2,3) and relaxation (type-1,2) sequences. Once DW reaches sufficiently close to the grain boundary, the R2 domain becomes very narrow. At this point, it is important to mention that half of the DW width has  $P_n < 0$  near the R2 region and another half near the R1 domain has  $P_n > 0$ . The notation of "half of the DW width  $(DW_{1/2})$ " implies the DW region within which polarization varies either from "0" to " $+|P_{n,r}|$ " (in the R1 side) or from 0 to " $-|P_{n,r}|$ " (in the R2 side). Interestingly, at some point, as the DW approaches the grain edges, the R2 domain can become narrow and the DW region on the side of R2 becomes less than  $DW_{1/2}$ . In that case, the variation of  $P_n$  becomes restricted within the narrower region than the typical DW<sub>1/2</sub>. Therefore, the term  $\nabla^2 P_n$  increases within the R2 domain yielding  $|E_n^{int}| > 1$ . Therefore, the R2 domain exhibits an effective outward force which leads to a spontaneous polarization switching in the R2 domain near the grain edge, as shown in Fig. 3(bv-vi). Therefore, when the R2 domain approaches the grain edge, spontaneous P-relaxation is not observed in the absence of the Efield (during  $T_{off}$ ). Instead, spontaneous P-excitation {Fig. 3[av(a)-vi] takes place. After all the lattices switch to  $+|P_{n,r}|$ , transient  $\bar{P}_n$  exhibits only type-2 excitation and relaxation.

Let us define the increase in  $\bar{P}_n$  during each excitation period  $(|\Delta^+\bar{P}_n|_i)$ . Recall that each  $|\Delta^+\bar{P}_n|_i$  consists of three excitation

components. It can be shown mathematically from Eq. (1) (see supplementary material) that the P change due to type-1 excitation is higher in magnitude than that due to type-2 excitation [Fig. 3(c)]. Now, with the increase in the pulse number (j), the R1 area increases and the R2 area decreases. Therefore, the contribution from type-2 excitation (in R1) increases and that from type-1 excitation (in R2) decreases. Hence, we expect an overall decrease in total excitation (type-1+2) with respect to j. Now, for type-3 excitation (corresponding to the R1 area increase during the *j*-th excitation)  $\Delta A_i^+ = \pi [(r_i + dr_i)^2]$  $-r_i^2$ ] =  $\pi[dr_i^2 + 2r_idr_i]$ . Here,  $r_i$  is the domain radius before the j-th excitation and  $dr_i$  is the increase in radius during the j-th excitation. Note that a linear increase in  $dr_i$  with respect to time gives rise to a quadratic increase in the R1 area. This implies that if we keep the Epulse ON for a long time, the  $\bar{P}_n$  dynamics will be quadratic with respect to time [gray lines in Fig. 3(a)]. Similarly, assuming  $dr_i$  as constant irrespective of the value of j, we can see that  $\pi \times 2r_i dr_i$  increases with j as  $r_i$  increases. This implies an incremental change in  $\Delta A_i^+$ , and hence, the type-3 excitation component increases with j. Note that the type-3 contribution is dominant over type-1+2, and therefore,  $|\Delta^+ \bar{P}_n|_i$  increase with the increase with j up to j = 6 [Fig. 3(d)]. For j > 6, the R1 domain reaches the grain boundary and the quadratic growth of R1 no longer holds true. Hence, type-3 contribution decreases significantly, leading to the domination of type-1 + 2 excitations and decrease in  $|\Delta^+ \bar{P}_n|_i$  with j. After the R2 domain vanishes (or switched to +P at j = 9), only type-2 excitation is observed.

Similarly, the decrease in  $\bar{P}_n$  during each relaxation period  $(|\Delta^-\bar{P}_n|_j)$  consists of type-1 + 2 relaxation and a spontaneous component. Like type-1 + 2 excitation, type-1 + 2 relaxation decreases as j increases. However, the spontaneous component  $(\Delta A_j^-)$  behaves nonmonotonically with respect to j.  $\Delta A_j^-$  (decrease in the R1 area) changes sign from positive (+) to negative (-) at j=6 as the spontaneous component changes from relaxation to excitation characteristics. Therefore, until the spontaneous contribution is relaxation ( $j \leq 6$ ),  $|\Delta^-\bar{P}_n|_j$  decreases with the increase in j. Once the spontaneous contribution leads to excitation (j > 7),  $|\Delta^-\bar{P}_n|_j$  increases with j and becomes constant at j=9 (with only type-2 relaxation in R1).

 $ar{P}_n$  at the end of each excitation-relaxation sequence, called accumulated polarization  $(P_n^{acc})$ , is shown in Fig. 3(a). Note that the change in  $P_n^{acc}$  at each pulse is proportional to  $\Delta A_j^+ - \Delta A_j^-$ . We discussed earlier that  $\Delta A_j^+$  shows an incremental increase with the increase in j, whereas  $\Delta A_j^-$  exhibits a nonmonotonic change along with a sign change from "+" to "-". Therefore,  $P_n^{acc}$  initially increases slowly when  $\Delta A_j^-$  is + and once  $\Delta A_j^-$  becomes -,  $P_n^{acc}$  increases rapidly. On the other hand, the flat region [Fig. 3(a),  $j \geq 9$ ] in  $P_n^{acc}$  signifies an absence in P-accumulation once the whole sample (or grain) completely switches to +P.

The trends in P accumulation with respect to the pulse attributes are illustrated in Figs. 3(e)-3(g). With the increase in the pulse amplitude ( $E_{n,max}^{app}$ ), the R1 domain grows more rapidly (increase in  $dA^+/dt$ ), leading to faster accumulation [Fig. 3(e)]. Similarly, with the increase in  $T_{on}$ ,  $\Delta A_j^+$  increases during each pulse, and therefore,  $P_n^{acc}$  saturates at a lower j [Fig. 3(f)]. Also, an increase in  $T_{off}$  leads to an increase in spontaneous relaxation (increase in  $\Delta A_j^-$ ). Consequently, a larger number of pulses are required for  $P_n^{acc}$  to saturate [Fig. 3(g)]. Note that if  $E_{n,max}^{app}$  and/or  $T_{on}$  are/is very low, so that  $(\Delta A_j^+ - \Delta A_j^-) < 0$ , then, rather than accumulation, R1 can get completely relaxed to -P. The same is true for a high  $T_{off}$ . Such scenarios can be seen in Figs.

3(e)–3(g) (gray lines). Note here that we assume the pinned (or initially nucleated) domain at the center of the grain. However, depending on the position of the pinned domain, the pulse number (*j*) corresponding to the spontaneous relaxation/excitation may vary, while retaining the overall accumulative nature in *P*-switching dynamics (see supplementary material).

Now, we consider case-2, where we assume a Gaussian distribution of the coercive field  $(E_C)$  in an FE grain [Fig. 4(a)] by considering a spatial distribution of  $\hat{\alpha}$ ,  $\hat{\beta}$ , and  $\hat{\gamma}$  (see supplementary material). Note that  $E_C$  is assumed to be less near the grain boundary [Fig. 4(b)], which can be understood as the cause of strain relaxation near the edges.<sup>24,25</sup> Like the previous discussion, considering a sequence of Efield pulses ( $E_{n,max}^{app} = 0.92$ ), simulated  $\bar{P}_n$  is shown in Fig. 4(c). Note that the FE grain was initially switched to  $-|P_{n,r}|$  [Fig. 4(d-i)]. Therefore, P-switching occurs as a two-step process: (1) E-field induced nucleation and (2) E-field assisted domain growth. Once the first E-field pulse arrives, direct nucleation starts from the grain edges (with lower  $E_C$ ) and propagates inward [Fig. 4(d-ii)]. After the end of the E-field pulse, further nucleation stops and type-1-2 relaxation takes place {Fig. 4[c-ii-ii(a)]} followed by a spontaneous relaxation {Figs. 4[c-ii(a)-iii] and 4(d-iii)} due to DW instability. However, after the 3rd pulse (j > 3), spontaneous excitation occurs in the absence of the E-field {Fig. 4[c-v(a)-vi]}, rather than spontaneous relaxation. Note that the origin of spontaneous excitation in this case is not the instability of DW near the grain boundary. In contrast, when two DWs are sufficiently close (distance being less than the DW width), then the intermediate domain experiences the addition of two  $E_n^{int}$ components governed by both the DWs. Therefore, total  $E_n^{int} > 1$  at DW interfaces alongside the intermediate domain. Consequently, the intermediate domain becomes unstable and spontaneously switches to + P [Fig. 4(d-v-vi)]. Such spontaneous excitation continues up to j=4, until all the lattices have switched to +P. The corresponding  $|\Delta^+ \bar{P}_n|_i$ ,  $|\Delta^- \bar{P}_n|_i$ , and  $P_n^{acc}$  values are shown in Figs. 4(e)-4(h) that present similar trends like case-1. However, an important difference between these two cases is stronger spontaneous excitation and relaxation in case-2 compared to that in case-1 (see supplementary material for details), which yields relatively abrupt *P*-switching in case-2.

With the understanding of P-excitation/relaxation processes in an FE grain, we now analyze the P-accumulation in HZO by considering an ensemble of grains. The global  $E_C$  distribution for HZO (80  $\mu$ m  $\times$  80  $\mu$ m) is shown in Fig. 5(a), which we extract from the measured P-E curves (see supplementary material). Then, we use each sampled  $E_C$  as the mean value of a local Gaussian distribution of  $E_C$  in a grain (like case-2). Considering a large number of grains, the global distribution of  $E_C$  is shown in Fig. 5(a).

By considering a sequence of E-field pulses (for  $E_{n,max}^{app} = 0.8, 1.0$ , and 1.2), simulated  $\bar{P}_n$  and corresponding  $P_n^{acc}$  are shown in Figs. 5(b) and 5(c). While the signatures of the dynamics of the single grain (discussed above) are manifested in HZO (ensemble of grains), two important differences can be observed in HZO: (1) saturation of accumulated P occurs at an intermediate value which increases for higher  $E_{n,max}^{app}$ , higher  $T_{on}$  and or lower  $T_{off}$  [Figs. 5(c)–5(e)] and (2) for a long relaxation time, the overall P does not relax completely [Fig. 5(b): gray dashed lines]. The former observation is attributed to two processes. First, grains with low mean  $E_C$  switch completely after a sufficient number of pulses and therefore do not contribute to P accumulation further, leading to intermediate saturation. Second, grains with

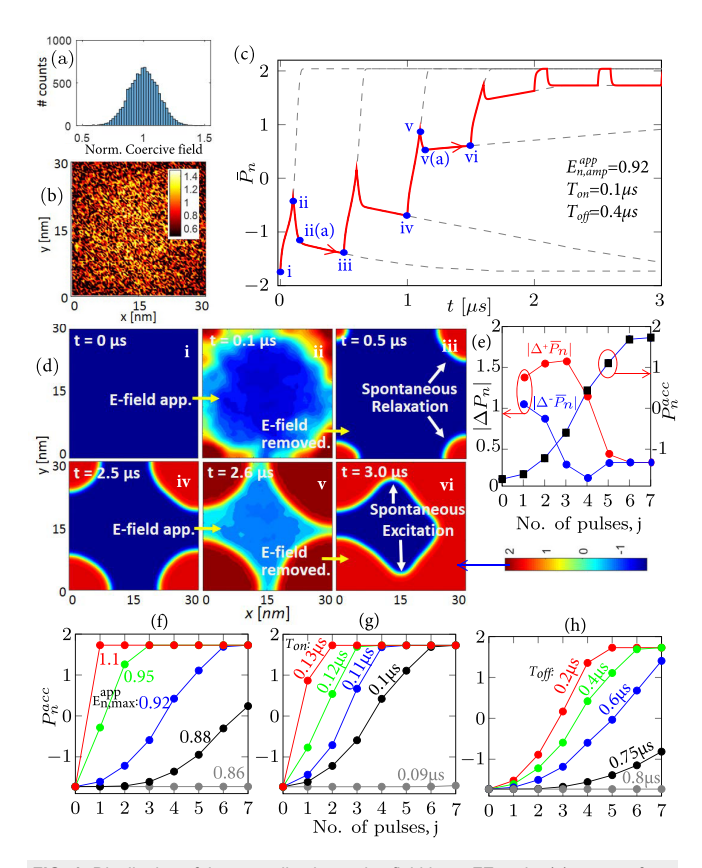


**FIG. 4.** Distribution of the normalized coercive field in an FE grain, (a) as area fraction and (b) as spatial. (c) Simulated transient  $\bar{P}_n$ . Corresponding (d) P-map at points i–vi, (e)  $|\Delta^+\bar{P}_n|$ ,  $|\Delta^-\bar{P}_n|$ , and  $P_n^{acc}$  with respect to j.  $P_n^{acc}$  vs j for different (f)  $E_{n,max}^{app}$ , (g)  $T_{on}$ , and (h)  $T_{off}$ . Here,  $E_{n,max}^{app} = E_{max}^{app} / E_{CO}$ .

sufficiently high mean  $E_C$  exhibit low initial nucleation for given  $E_{n,max}^{app}$  and  $T_{on}$ . Therefore, given a relaxation time, the grains with higher  $E_C$  are more likely to relax completely and hence do not participate in *P*-accumulation. Now, with the increase in  $E_{n,max}^{app}$  and  $\bar{T}_{on}$ , initial nucleation is enhanced, reducing the probability of complete relaxation in high  $E_C$  grains. A decrease in  $T_{off}$  also has a similar effect on relaxation. Therefore, a larger number of grains contribute to Paccumulation, leading to a saturation at higher P [Figs. 5(c)-5(e)]. The second observation (incomplete relaxation for large  $T_{off}$ ) can be attributed to the completely switching of low mean  $E_C$  grains during the excitation and hence, do not contribute to spontaneous relaxation. Note that the large distribution of  $E_C$  corresponds to the large area of our fabricated HZO sample. However, by scaling the area of HZO, a lower number of grains can be achieved. Therefore, the P-accumulation of a scaled HZO should exhibit a lower number of saturation levels as well as more prominent spontaneous P-excitation/relaxation characteristics.

In summary, we experimentally demonstrated the accumulative *P*-switching in HZO. Then, developing a phase-field model, we discuss the *P*-switching dynamics by analyzing different stimulated and spontaneous *P*-excitation/relaxation mechanisms governed by the domain-domain interaction and DW instability. We attribute the strength and directional change in DW instability as one of the key factors for

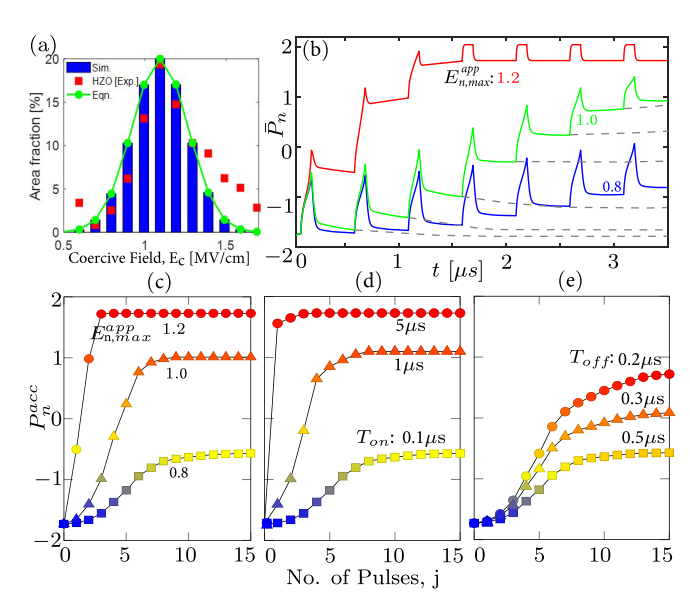


**FIG. 5.** (a) Coercive field,  $E_{C}$ , distribution in HZO: (red) experiment; (blue/green) used for simulation. (b) Simulated transient  $\bar{P}_n$  for different  $E_{n,max}^{app}$ .  $P_n^{acc}$  vs j for different (c)  $E_{n,max}^{app}$ , (d)  $T_{on}$ , and (e)  $T_{off}$ .

accumulative *P*-switching. Finally, considering an inter/intragrain coercive-field distribution in our simulations, we describe the experimentally observed accumulative *P*-switching in HZO.

See the supplementary material for experimental calibration, parameter extraction, derivation of equations, and other relevant details.

This work was supported, in part, by NSF under Grant No. 1717999.

#### **REFERENCES**

<sup>1</sup>J. Muller, T. S. Boscke, U. Schroder, S. Mueller, D. Brauhaus, U. Bottger, L. Frey, and T. Mikolajick, Nano Lett. **12**, 4318 (2012).

<sup>2</sup>P. Sharma, K. Tapily, A. K. Saha, J. Zhang, A. Shaughnessy, A. Aziz, G. L. Snider, S. Gupta, R. D. Clark, and S. Datta, in 2017 Symposium on VLSI Technology (2017), pp. T154–T155.

<sup>3</sup>A. K. Saha, P. Sharma, I. Dabo, S. Datta, and S. K. Gupta, in 2017 IEEE International Electron Devices Meeting (IEDM) (2017), pp. 13.5.1–13.5.4.

<sup>4</sup>K. Chatterjee, S. Kim, G. Karbasian, A. J. Tan, A. K. Yadav, A. I. Khan, C. Hu, and S. Salahuddin, IEEE Electron Device Lett. 38, 1379 (2017).

<sup>5</sup>H. Mulaosmanovic, T. Mikolajick, and S. Slesazeck, ACS Appl. Mater. Interfaces 10, 23997 (2018).

<sup>6</sup>K. Ni, B. Grisafe, W. Chakraborty, A. K. Saha, S. Dutta, M. Jerry, J. A. Smith, S. Gupta, and S. Datta, in 2018 IEEE International Electron Devices Meeting (IEDM) (2018), pp. 16.1.1–16.1.4.

<sup>7</sup>H. Mulaosmanovic, E. Chicca, M. Bertele, T. Mikolajickac, and S. Slesazecka, Nanoscale 10, 21755 (2018).

<sup>8</sup>Y. L. Li, S. Y. Hu, Z. K. Liu, and L. Q. Chen, Appl. Phys. Lett. **78**, 3878 (2001).

9K. M. Rabe, C. H. Ahn, and J.-M. Triscone, Physics of Ferroelectrics—A Modern Perspective (Springer, 2007).

<sup>10</sup> A. K. Tagantsev, I. Stolichnov, N. Setter, J. S. Cross, and M. Tsukada, Phys. Rev. B 66, 214109 (2002).

<sup>11</sup>J. Wang and T.-Y. Zhang, Phys. Rev. B 73, 144107 (2006).

- <sup>12</sup>J. Wang, S.-Q. Shi, L.-Q. Chen, Y. Li, and T.-Y. Zhang, Acta Mater. 52, 749
- (2004).

  13 Y. Li, S. Hu, Z. Liu, and L. Chen, Acta Mater. 50, 395 (2002).

  14 M. Hoffmann, A. I. Khan, C. Serrao, Z. Lu, S. Salahuddin, M. Peisec, S. Slesazeck, U. Schroeder, and T. Mikolajick, J. Appl. Phys. 123, 184101 (2018).
- <sup>15</sup>A. K. Bandyopadhyay, P. C. Ray, and V. Gopalan, J. Phys.: Condens. Matter 18, 4093 (2006).
- <sup>16</sup>E. OConnor, M. Halter, F. Eltes, M. Sousa, A. Kellock, S. Abel, and J. Fompeyrine, APL Mater. 6, 121103 (2018).
- 17 R. Materlik, C. Knneth, and A. Kersch, J. Appl. Phys. 117, 134109 (2015).
   18 S. Nambu and D. A. Sagala, Phys. Rev. B 50, 5838 (1994).
- <sup>19</sup>R. Lynden-Bell, Mol. Phys. **86**, 1353 (1995).

- 20Q. Meng, M.-G. Han, J. Tao, G. Xu, D. O. Welch, and Y. Zhu, Phys. Rev. B 91, 054104 (2015).
- <sup>21</sup>Y. Gu, M. Li, A. N. Morozovska, Y. Wang, E. A. Eliseev, V. Gopalan, and L.-Q. Chen, Phys. Rev. B 89, 174111 (2014).
- <sup>22</sup>A. Cano and D. Jiménez, Appl. Phys. Lett. **97**, 133509 (2010).
- 23 E. A. Eliseev, A. N. Morozovska, G. S. Svechnikov, P. Maksymovych, and S. V. Kalinin, Phys. Rev. B 85, 045312 (2012).
- <sup>24</sup>A. Emelyanov, N. Pertsev, S. Hoffmann-Eifert, U. Böttger, and R. Waser, J. Electroceram. 9, 5 (2002).
- 25 J.-S. Lee, E.-C. Park, J.-H. Park, B.-I. Lee, and S.-K. Joo, Effects of Grain Boundary on the Ferroelectric Properties of Selectively Grown PZT Thin Films (Mater. Res. Soc. Proc., 1999), Vol. 596, p. 315.

#### **Supplementary Section**

## Phase Field Modeling of Domain Dynamics and Polarization Accumulation in Ferroelectric HZO

Atanu K Saha<sup>1</sup>, Kai Ni<sup>2</sup>, Sourav Dutta<sup>2</sup>, Suman Datta<sup>2</sup>, and Sumeet Gupta<sup>1</sup>

<sup>1</sup>Schooll of Electrical and Computer Engineering, Purdue University, West Lafayette, IN, USA

<sup>2</sup>Department of Electrical Engineering, University of Notre Dame, Notre Dame, IN, USA

#### **Phase-field Model:**

The spatial and temporal evolution of polarization (P) can be calculated from the following time-dependent Landau-Ginzburg (TDLG) equation [1-2].

$$\frac{\delta F}{\delta \mathbf{P}} = -\rho \frac{\partial \mathbf{P}}{\partial t} \tag{S1}$$

Here,  $\rho$  is the kinetic or viscosity coefficient, F is the total system energy and t is the time. We assume the polarization direction is only along the thickness (z-axis) of the FE i.e.  $P_x=0$ ,  $P_y=0$ ,  $P_z\neq0$ . Taking into account different energy density terms (free energy, domain-wall energy, and electrostatic energy and eleastic) into account, eqn. (S1) can be written as [3-4],

$$-\rho \frac{dP_Z}{dt} = -E_Z^{app} - K_P \nabla^2 P_Z + \alpha P_Z + \beta P_Z^3 + \gamma P_Z^5$$
 (S2)

Here,  $E_Z^{app}$  is the applied electric field (E-field) along the z-axis and  $K_P$  is the domain coupling parameter. Now, by assuming uniform polarization distribution ( $\nabla^2 P_Z = 0$ ) and static condition ( $dP_Z/dt=0$ ), we plot the  $P_Z$  vs  $E_Z^{app}$  characteristics (according to eqn. (S2)) and the corresponding  $P_Z$  vs  $dE_Z^{app}/dP_Z$  curve in Fig. S1(a) (for  $\alpha < 0$ ,  $\beta > 0$  and  $\gamma > 0$ ). Now, let us define the microscopic coercive field ( $E_{C0}$ ) as the applied E-field at which  $dE_Z^{app}/dP_Z = 0$  and the corresponding polarization as  $P_{C0}$  (see Fig. S1(a)). Normalizing the applied E-field with respect to  $E_{C0}$  and polarization with respect to  $P_{C0}$ , we can write eqn. (S2) as the following equation.

$$-\frac{\rho P_C}{E_{C0}} \frac{d\left(\frac{P_Z}{P_{C0}}\right)}{dt} = -\frac{E_Z^{app}}{E_{C0}} - \frac{K_p P_{C0}}{E_{C0}} \nabla^2 \left(\frac{P_Z}{P_{C0}}\right) + \frac{\alpha P_{C0}}{E_{C0}} \left(\frac{P_Z}{P_{C0}}\right) + \frac{\beta P_{C0}^3}{E_{C0}} \left(\frac{P_Z}{P_{C0}}\right)^3 + \frac{\gamma P_{C0}^5}{E_{C0}} \left(\frac{P_Z}{P_{C0}}\right)^5 \tag{S3}$$

Eqn. (S3) can further be written as

$$-\rho_n \frac{dP_n}{dt} = -E_n^{app} - K_P^n \nabla^2 P_n + \hat{\alpha} P_n + \hat{\beta} P_n^3 + \hat{\gamma} P_n^5$$
 (S4)

Here, 
$$P_n = \frac{P_Z}{P_{C0}}$$
,  $\rho_n = \frac{\rho P_{C0}}{E_{C0}}$ ,  $E_n^{app} = \frac{E_Z^{app}}{E_{C0}}$ 

Now, we derive the relations among normalized Landau coefficients  $(\hat{\alpha}, \hat{\beta} \text{ and } \hat{\gamma})$  for a given value of normalized remnant polarization  $(P_{n,r} = P_R/P_{C0}, P_R = \text{unnormalized remnant polarization})$ . To do so, we consider steady state  $(\frac{dP_n}{dt} = 0)$  and homogeneous  $P_n$ , therefore,  $\nabla^2 P_n = 0$ . Hence, eqn. (S4) can be written as the following equation by considering the static condition  $(\frac{dP_n}{dt} = 0)$ .

$$E_n^{app} = \hat{\alpha} P_n + \hat{\beta} P_n^3 + \hat{\gamma} P_n^5 \tag{S5}$$

Note that, in the normalized space, coercive field  $(E_{n,c}) = \pm 1$  and at the coercive field  $(E_n^{APP} = E_{n,c})$ , normalized polarization,  $P_n = P_{n,c} = \mp 1$ . Therefore, by putting  $E_n^{APP} = 1$  and  $P_n = -1$  in eqn. (S5), we can write,

$$\hat{\alpha} + \hat{\beta} + \hat{\gamma} = -1 \tag{S6}$$

Also,  $dE_n/dP_n = 0$  at  $P_n = P_{n,c} = \mp 1$  (see Fig. S1(a)), therefore,

$$\hat{\alpha} + 3\hat{\beta}P_n^2 + 5\hat{\gamma}P_n^4 = \frac{dE_n}{dP_n}$$

$$\hat{\alpha} + 3\hat{\beta} + 5\hat{\gamma} = 0 \tag{S7}$$

Solving eqn. (S6) and eqn. (S7), we can write,

$$\hat{\alpha} = \hat{\gamma} - \frac{3}{2}$$
 (S8)  
$$\hat{\beta} = -2\hat{\gamma} + \frac{1}{2}$$
 (S9)

$$\hat{\beta} = -2\hat{\gamma} + \frac{1}{2} \tag{S9}$$

Now, putting the value of  $\hat{\alpha}$  and  $\hat{\beta}$  in eqn. (S5), we can write,

$$E_n^{APP} = (\hat{\gamma} - \frac{3}{2})P_n + (-2\hat{\gamma} + \frac{1}{2})P_n^3 + \hat{\gamma}P_n^5$$

At  $E_n^{APP} = 0$ ,  $P_n = P_{n,r}$ , therefore,

$$0 = \left(\hat{\gamma} - \frac{3}{2}\right) P_{n,r} + \left(-2\hat{\gamma} + \frac{1}{2}\right) P_{n,r}^3 + \hat{\gamma} P_{n,r}^5$$

$$\hat{\gamma} = -\frac{\frac{1}{2}(P_{n,r}^2 - 3)}{(P_{n,r}^2 - 1)^2}$$
 (S10)

Now, by normalizing the experimentally measured P-E characteristics with respect to  $E_C$ ,  $P_C$  and getting the corresponding  $P_{n,r}$ , we calculate the normalized Landau coefficients from eqn. (S8)-(S10). The calibration is shown in Fig. S1(b) and that provides  $\hat{\alpha} = -1.499, \hat{\beta} = 0.498$  and  $\hat{\gamma} = 0.001$ . In our phase-field simulation, we use  $K_p^n = 1$ .

Now, if we consider a non-homogeneous distribution of  $E_C(E_{n,c})$  exhibits spatial variation) in an FE grain, then by following a similar approach, we can derive the following set of equations. Note,  $E_{n,c}$ , here, is a random variable with mean = 1)

wing set of equations. Note, 
$$E_{n,c}$$
, here, is a  $\hat{\gamma} = -\frac{\frac{1}{2}(E_{n,c}P_{n,r}^2 - 3E_{n,c})}{(P_{n,r}^2 - 1)^2}$  (S14) 
$$\hat{\alpha} = \hat{\gamma} - \frac{3}{2}E_{n,c}$$
 (S15)

$$\hat{\beta} = -2\hat{\gamma} + \frac{1}{2}E_{n,c} \qquad (S16)$$

Now, we can calculate the distribution in  $\hat{\alpha}$ ,  $\hat{\beta}$  and  $\hat{\gamma}$  from eqn. (S14)-(S16) for a Gaussian distribution in  $E_{n,c}$  (mean = 1 and standard deviation = 0.125). To do so, we assume constant  $P_{n,r}$  and calculate  $\hat{\alpha}$ ,  $\hat{\beta}$  and  $\hat{\gamma}$  by capturing the variation in  $E_{n,c}$ . LGD equation (4) with  $\hat{\alpha}$ ,  $\hat{\beta}$  and  $\hat{\gamma}$  treated as random variable is solved to simulate the dynamics of polarization switching in this work.

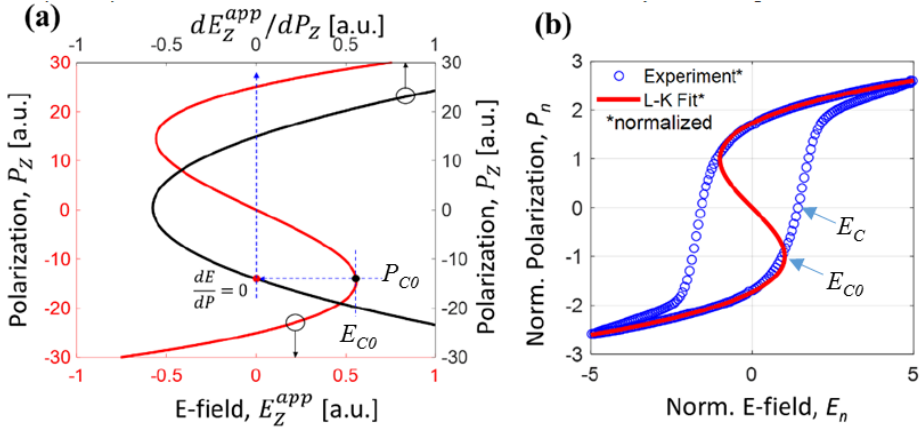


**Fig. S1:** (a) Polarization ( $P_Z$ ) vs E-field ( $E_Z^{app}$ ) (red) and  $P_Z$  vs  $dE_Z^{app}/dP_Z$  characteristics (black) according to eqn. (S2) by assuming homogeneous  $P_Z$ -distribution and static condition. (b) Calibration of model parameters (Landau coefficients) with experiment in normalized space.  $[\hat{\alpha} = -1.499, \hat{\beta} = 0.498 \text{ and } \hat{\gamma} = 0.001]$ , we use  $K_p^n = 1.0$  in all the simulations.

#### Note:

In general, the definition of ' $E_C$  is the electric field where P is zero' is for average polarization that corresponds to a macroscopic definition of coercive field. Here,  $E_{C0}$  is for a single lattice/grid point (microscopic coercive field). From the perspective of polarization switching,  $E_{C0}$  serves as the threshold E-field responsible for polarization switching in a single lattice. Note, the distinction between  $P_C$  and  $P_{C0}$  is that  $P_{C0}$  (microscopically polarization cannot be zero) is not 0, while  $P_C$  (due to the definition of macroscopic  $E_C$ ) is 0.

Note, in the un-normalized state,  $|P_r| > |P_{C0}|$ .  $P_{C0} = \sim 15 \mu C/cm^2$  and  $P_R \sim 25 \mu C/cm^2$ After normalization,  $|P_{n,C0}| = 1$  and therefore,  $|P_{n,r}| \approx (25/15) = \sim 1.7$ .

#### **Polarization Excitation and Relaxation:**

Any increase in microscopic polarization from its remanent value  $(P_{n,r})$  can be considered as the 'P-excitation', where a decrease can be denoted as the 'P-relaxation'. Due to an applied electric field, stimulated increase in polarization occurs and can be referred as 'P-excitation'. In a homogeneous mono-domain scenario (in absence of a DW), if the applied field is less than the coercive field, the polarization changes either (i) from  $-|P_{n,r}|$  to  $-|P_{n,e1}|$  or (ii) from  $+|P_{n,e2}|$ . Here, we refer such P-excitation as type-1 and type-2, respectively. When the applied electric field is removed, the polarization returns to its remanent value either (i) from  $-|P_{n,e1}|$  to  $-|P_{n,e1}|$  to  $+|P_{n,e2}|$  to  $+|P_{n,r}|$ . Such decrease in polarization can be referred as type-1 and type-2 'P-relaxation', respectively. Physically, the type-1 and type-2 excitation/relaxation components can be understood as the electric field driven soft dielectric [6] type capacitive charging/discharging event, where type-1 and type-2 excitation/relaxation occur in domains with the remnant polarization of  $-|P_{n,r}|$  and  $+|P_{n,r}|$ , respectively. Here, soft dielectricity means the change in dipole moment (dP/dE) due to an applied E-field without any polarization switching.

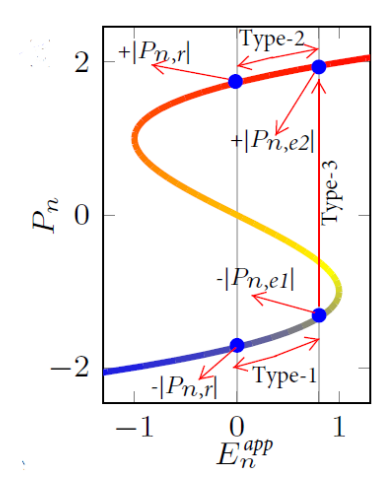


Fig S2.  $P_n$  versus  $E_n^{app}$  relation showing type-1 and type-2 excitation and relaxation components.

Here, type-1 excitation implies a change from  $-|P_{n,r}|$  to  $-|P_{n,e1}|$  and type-2 excitation implies  $+|P_{n,r}|$  to  $+|P_{n,e2}|$  as shown in the Fig. S2. According to Landau equation, the polarization  $(P_n)$  and electric field  $(E_n^{app})$  relation can be written as,

$$\begin{split} E_n^{app} &= \hat{\alpha} P_n + \hat{\beta} P_n^3 + \hat{\gamma} P_n^5 \quad \text{(S17)} \\ \frac{dE_n^{app}}{dP_n} &= \hat{\alpha} + 3\hat{\beta} P_n^2 + 5\hat{\gamma} P_n^4 \end{split}$$

From the last equation, the differential change in polarization can be written as,

$$\frac{dP_n}{dE_n^{app}} = \frac{1}{\widehat{\alpha} + 3\widehat{\beta}P_n^2 + 5\widehat{\gamma}P_n^4} \quad (S18)$$

Note that, the type-1 and type-2 excitation components ( $\Delta P_n^{type-1}$  and  $\Delta P_n^{type-2}$ ) can be represented as the differential change in polarization due to an applied electric field and can be written as following equations.

$$\Delta P_n^{type-1(2)} = \int_0^{E_n^{app}} \frac{dP_n}{dE_n^{app}} dE_n^{app} (S19)$$

Note that, at  $E_n^{app}=0$ ,  $P_n=\pm |P_{n,r}|$ , the quantity  $\frac{dP_n}{dE_n^{app}}$  is the same for  $P_n=\pm |Pr|$ .

It is important to note that, during type-1 excitation,  $|P_n|$  is decreasing  $(P_n)$  is becoming less negative) with the increase in  $E_n^{app}$  (can be seen from the figure). Therefore,  $\frac{dP_n}{dE_n^{app}}$  should increase (according to eqn. (S18)) with the increase in  $E_n^{app}$ .

On the other hand, during type-2 excitation,  $|P_n|$  is increasing with the increase in  $E_n^{app}$  (can be seen from the figure). Therefore,  $\frac{dP_n}{dE_n^{app}}$  should decrease (according to eqn. (S18)) with the increase in  $E_n^{app}$ .

The term  $\frac{dP_n}{dE_n^{app}}$  is increasing in case of type-1 excitation and is decreasing in case of type-2 excitation with the increase in  $E_n^{app}$ . Therefore, from eqn. (S19), we can see that  $\Delta P_n^{type-1} > \Delta P_n^{type-2}$ .

To get a numerical perspective of type-1 and type-2 excitation components, the calculated values of  $\pm |P_{n,r}|=1.7298$  for  $\hat{\alpha}=-1.499, \hat{\beta}=0.498$  and  $\hat{\gamma}=0.001$ . At  $E_n^{app}=0.8, |P_{n,e1}|=1.3450$  and  $|P_{n,e2}|=1.9505$ .

$$\begin{split} &\Delta P_n^{type-1} = |P_{n,r}| - |P_{n,e1}| = 1.7298 - 1.3450 = 0.3484 \\ &\Delta P_n^{type-2} = |P_{n,e2}| - |P_{n,r}| = 1.9505 - 1.7298 = 0.2207 \end{split}$$

Therefore,  $\Delta P_n^{type-1} > \Delta P_n^{type-2}$ .

#### Polarization switching considering 1D domain dynamics:

In general, P-switching can take place if  $|E_n^{int} + E_n^{app}| > 1$ . Here,  $E_n^{int}$  is the interaction E-field ( $= K_P^n \nabla^2 P_n$ ) and  $E_n^{app}$  is the applied E-field. In the main text, we discussed that the 1D domain-wall (DW) is stable due to the spatial symmetric nature of  $E_n^{int}$  and therefore,  $E_n^{int} \le 1$ . In other words, the DW is static when no electric field is applied ( $E_n^{app} = 0$ ). However, P-switching can be induced by applying an E-field,  $E_n^{app} > 0$ . Such  $E_n^{app} > 0$  causes  $E_n^{int} + E_n^{app} > 1$  and that initiates local nucleation near the DW, where  $|E_n^{int}| > 0$ .

Considering a sequence of E-field pulses (Fig. S3(a)), simulated transient  $\bar{P}_n$  is shown in Fig. S3(b) (solid red line). The initial P-map at t=0 has been shown in Fig. S3(e)-i. After the application of first E-field pulse, the DW will propagate along the +x-axis nucleating new lattices sequentially at the right edge of the DW. That implies an increase in R1 area (red region in Fig. S3(e)) and decrease in R2 area (blue region in Fig. S3(e)) by an amount of  $\Delta A_j^+ = w \times \Delta l_j$ , where  $\Delta l_j$  is the increase in length of R1 at j-th pulse and w is the width of the sample. The P-map at the end of the E-field pulse (at  $t=T_{on}$ ) is shown in Fig. S3(e)-ii. The corresponding transient excitation in  $\bar{P}_n$  can be seen in Fig. S3(b) (from point it to ii). This P-excitation can be attributed to three different contributions of change in polarization, i.e. type-1, type-2 and type-3 (discussed in the main text for 2D). After the end of first E-field pulse, the DW propagation stops and type-1 and 2 relaxations occur. Corresponding transient relaxation in  $\bar{P}_n$  can be seen in Fig. S3(b) (from point ii to iii) and P-map at the end of relaxation (at  $t=T_{on}+T_{off}$ ) has been shown in Fig. S3(e)-iii. Now, in the subsequent E-field pulses, the DW moves further along the +x-axis by following sequential P-excitation and relaxation sequences and finally switches all the lattices to +P. After that, transient  $\bar{P}_n$  exhibits only type-2 P-excitation and relaxation, which can be seen in Fig. S3(b) for j >8.

Note that, the 1D DW is stable in absence of an applied E-field (as we discussed earlier). To verify this argument, we simulate the transient polarization characteristics by considering long relaxation time after different excitation sequences (the corresponding E-field pulses are shown in Fig. S3(c)). Resultant transient  $\bar{P}_n$  is shown in Fig. S3(b) as dashed line showing no spontaneous P-relaxation in case 1D DW motion based P-switching. However, when the DW reaches very close to the grain boundary, the DW becomes unstable and can spontaneously collapse (similar to the 2D case discussed in the main text) along the grain edges leading to spontaneous P-excitation (Fig. S3(b) at sixth relaxation sequence). Increase in  $\bar{P}_n$  (called  $\Delta^+ P_n$ ), decrease in  $\bar{P}_n$  (called  $\Delta^- P_n$ ) and  $\bar{P}_n$  at the end of each excitation-relaxation sequence (called accumulated polarization,  $P_n^{acc}$ ) have been shown in Fig. S3(f).  $P_n^{acc}$  shows a linear increase w.r.t. the number of E-field pulses (j), which is due to the 1D degrees of freedom of DW motion that gives rise to equal  $\Delta A_j^+$  ( $\Delta I_j$  is constant irrespective of the pulse number) in each pulse. That implies, in case of 1D DW motion based P-switching, increase in polarization is linear with respect to time. To verify this argument, we simulate the transient polarization characteristics by considering long excitation time at different sequences (the corresponding E-field pulses are shown in Fig. S3(d)). Resultant transient  $\bar{P}_n$  is shown in Fig. S3(b) as dash-dotted line showing linear increase in  $\bar{P}_n$  till the saturation.

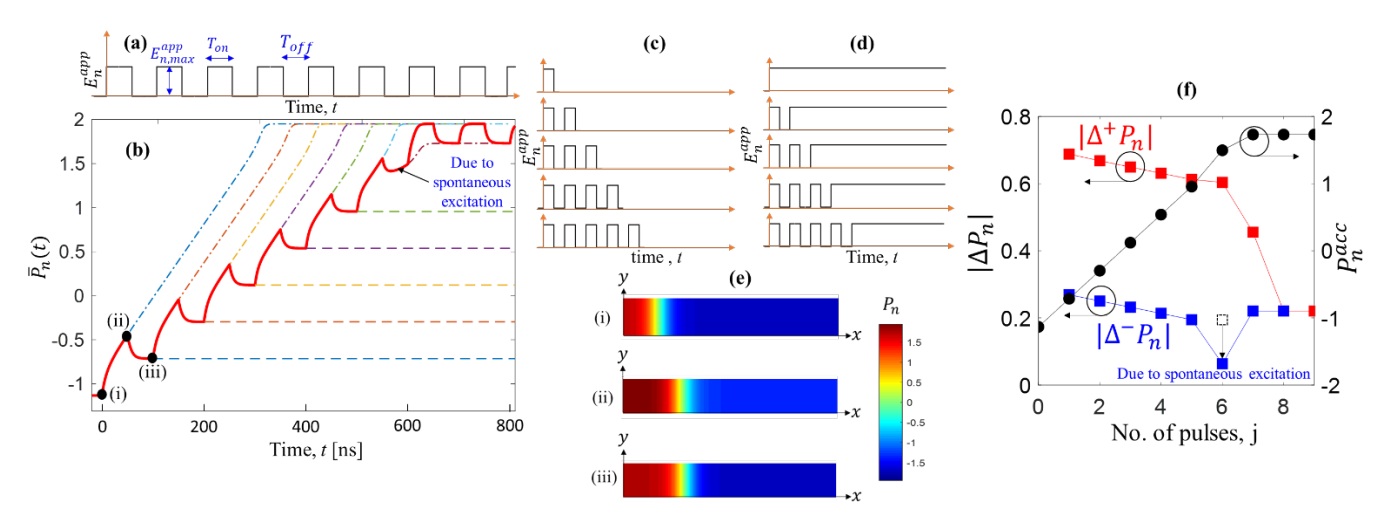


Fig. S3: Polarization switching dynamics considering 1D DW motion: (a) Applied E-field pulse sequences ( $E_{n,max}^{app} = 0.8$ ,  $T_{on} = 50ns$ ) and (b) resultant transient  $P_n$  (solid red). Applied E-field pulse sequences for prolonged (c) relaxation and (d) excitation characteristics and corresponding transient  $P_n$  are shown in (b) as dash-dotted line (for excitation) and dashed line (for relaxation). (e) P-map at point (i), (ii) and (iii) as marked in (b). Increase and decrease in  $P_n$  (respectively  $|\Delta^+P_n|$  and  $|\Delta^-P_n|$ ) and accumulated  $P_n$  ( $P_n^{acc}$ ) in each excitation/relaxation sequence with respect to pulse number (j).

Now, to analyze the effects of  $E^{app}_{n,max}$ , Ton and Toff in P-excitation/relaxation and accumulation characteristics, we plot the transient  $\bar{P}_n$  in Fig. S4(a-c) and  $P^{acc}_n$  with respect to the number of pulses (j) in Fig. S4(d-f) for different  $E^{app}_{n,max}$ ,  $T_{on}$  and  $T_{off}$ .  $\bar{P}_n$  shows higher P-excitation (in Fig. S4(a)) with higher  $E^{app}_{n,max}$  which can be understood as the increase in type-1 and type-2 excitation components and higher growth rate in R1 domain (increase in dlj/dt) with the increase in  $E^{app}_{n,max}$ . Higher P-excitation with the increase in  $E^{app}_{n,max}$  leads to faster P-accumulation w.r.t the pulse number (Fig. S4(d)). Similarly, an increase in  $T_{on}$  provides increased amount of forward nucleation (increase in  $\Delta l_j$ , while dlj/dt remains constant) and hence, increased  $\bar{P}_n$  during each E-field pulses (Fig. S4(b)). Therefore,  $P^{acc}_n$  requires relatively a smaller number of E-field pulses to reach the saturation point (Fig. S4(e)) for higher  $T_{on}$ . However, increase in  $T_{off}$  does not provide any change in  $\bar{P}_n$  and  $P^{acc}_n$  characteristics (Fig. S4(c) and in Fig. S4(f)) due to the absence of spontaneous P-relaxation process in case of 1D domain dynamics.

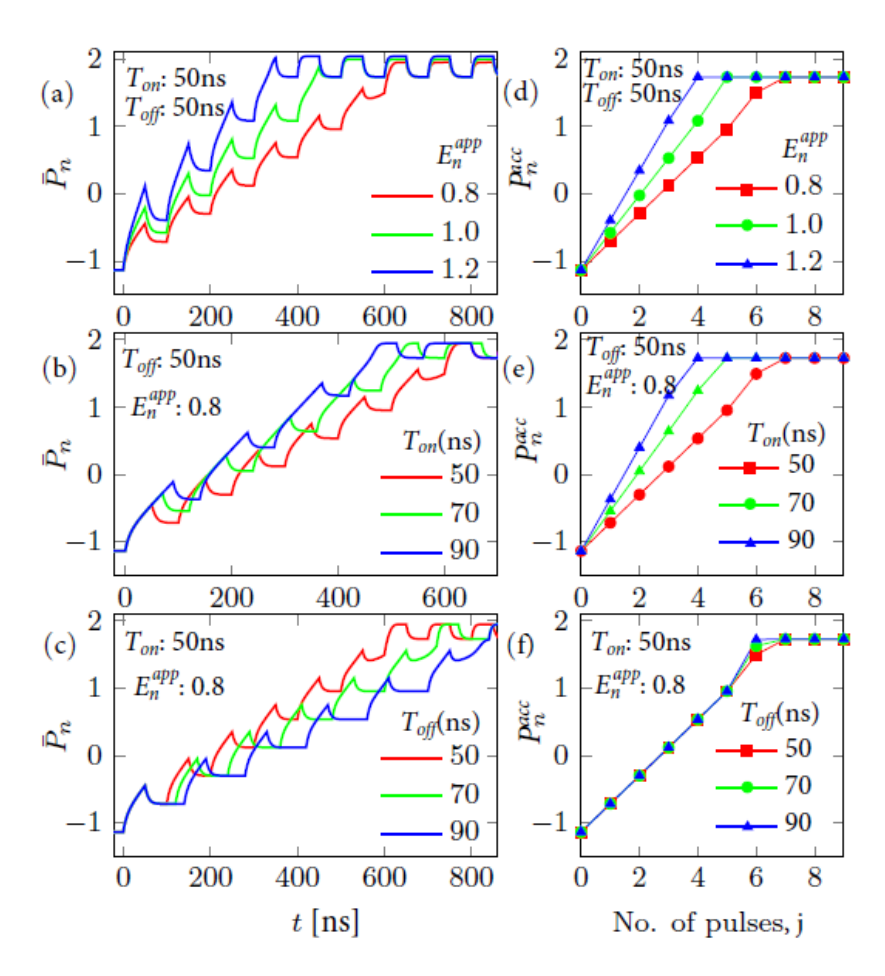


Fig. S4: Polarization switching dynamics considering 1D DW motion: transient  $P_n$  for different (a)  $E_{n,max}^{app}$  (magnitude of the applied E-field pulse), (b)  $T_{on}$  (excitation time) and (c)  $T_{off}$  (relaxation time); Accumulate polarization ( $P_n^{acc}$ ) with respect to the pulse number (j) for different (d)  $E_{n,max}^{app}$ , (e)  $T_{on}$  and (f)  $T_{off}$ . Here, we consider 1D domain-wall (DW) motion.

#### Differences between 1D and 2D DW motion based P-switching dynamics:

If the spatial distribution in polarization (P) is 1D, then the corresponding DW and their associated motion is also effectively 1D. In our main text, we discuss that the 1D DW is static and stable due to the spatially symmetric distribution of local effective interaction E-field ( $E_n^{int} = K_P^n \nabla^2 P_n$ ). Therefore, there will be no spontaneous DW motion (or P-switching) in absence of an applied E-field (unless the DW is sufficiently close to the grain boundary). At the same time, considering the E-field induced DW motion, the increase in polarization is linear with respect to time (due to linear increase in domain area). Consequently, the P-accumulation characteristics exhibits linear increase as a response of sequential E-field pulsing. However, in case of 2-dimentional polarization distribution, the corresponding 2D DW may not be stable due to spatially asymmetric nature of  $E_n^{int}$  and can exhibit spontaneous motion leading to spontaneous P-switching (relaxation or excitation, depending on the position of DW). In addition, as a response of sequential E-field pulsing, the increase in polarization is incremental with respect to time due to non-linear growth of domain area. For example, domain growth is quadratic for case-1 (main text), where we assume circular pinned domain at the center of the grain. Moreover, such incremental domain growth in case of 2D DW motion leads to relatively more accumulative and abrupt P-switching characteristics compared to 1D DW motion.

#### P-switching dynamics (homogeneous $E_c$ ) depending on the location of the pinned domain:

In the main text, we discuss the P-switching dynamics in an FE grain by considering a homogeneous  $E_C$  distribution and a pinned type domain at the center of the grain (case-1 of the main text). To analyze the dependence of P-switching dynamics on the location of pinned domain, here we consider different initial location for the pinned domain and compare the results. Transient  $\bar{P}_n$  as a consequence of sequential E-field pulsing (Fig. S5(a)) is shown in Fig. S5(b) by assuming the initial location of the pinned domain at four different positions (as shown in Fig. S5(c)) within the square FE grain, i.e., case-i: at the center, case-ii: at the vertex, case-(iii): midway between the center and side, and case-(iv): midway between the center and vertex. Corresponding P-maps are shown in Fig. S5(d) at the end of each excitation and relaxation sequences. For all the cases (i, ii, iii and iv), P-accumulation takes place by following sequentially stimulated P-excitation and P-relaxation process, as discussed in the main text. For case-i and case-ii, in absence of E-field, we initially observe spontaneous P-relaxation (due to radial asymmetry in interaction E-field) up to a certain number of pulses and after that we observe spontaneous P-excitation (due to DW collapse at the grain edges) till the saturation. Now, in case-iii the pinned domain is near the grain edge. Therefore, the DW collapses near the grain edge at very early stage (during first relaxation sequence in this case) and leads to spontaneous growth of R1 domain along the grain edge. At the same time, the opposite face of the R1 domain (towards the inner side of the grain) spontaneously shrinks (due to radial asymmetry in interaction E-field). Due to these simultaneous domain growth and shrinking (at different regions of the R1 domain), initially, shrinking dominates over the growth. Therefore, the R1 domain area decreases spontaneously and as a consequence, we observe overall P-relaxation (Fig. S5(b)-blue curve) in absence of applied E-field till the third relaxation sequences. However, at the fourth relaxation sequence, spontaneous domain growth dominates over shrinking and hence, we observe an overall spontaneous P-excitation. At the same time, note that the curvature of the R1 domain (facing inwards) decreases and that leads to a decrease in interaction E-field asymmetry. In other words, the nature of the DW approaches that of 1D-DW motion. Therefore, no (or very low) spontaneous change in polarization takes place from fifth to seventh relaxation sequences. At the eighth relaxation sequence, DW collapse at the grain edge and reaches saturation polarization. Similar to case-iii, in case-iv the pinned domain is near the grain edge. However, in this case, within the simultaneous domain growth and shrinking (at different regions of the R1 domain), initially, growth dominates over the shrinking. As a consequence, we observe an overall spontaneous P-excitation (Fig. S5(b)-red curve) at the second relaxation sequence. After that, spontaneous P-relaxation dominates till the sixth relaxation sequences.

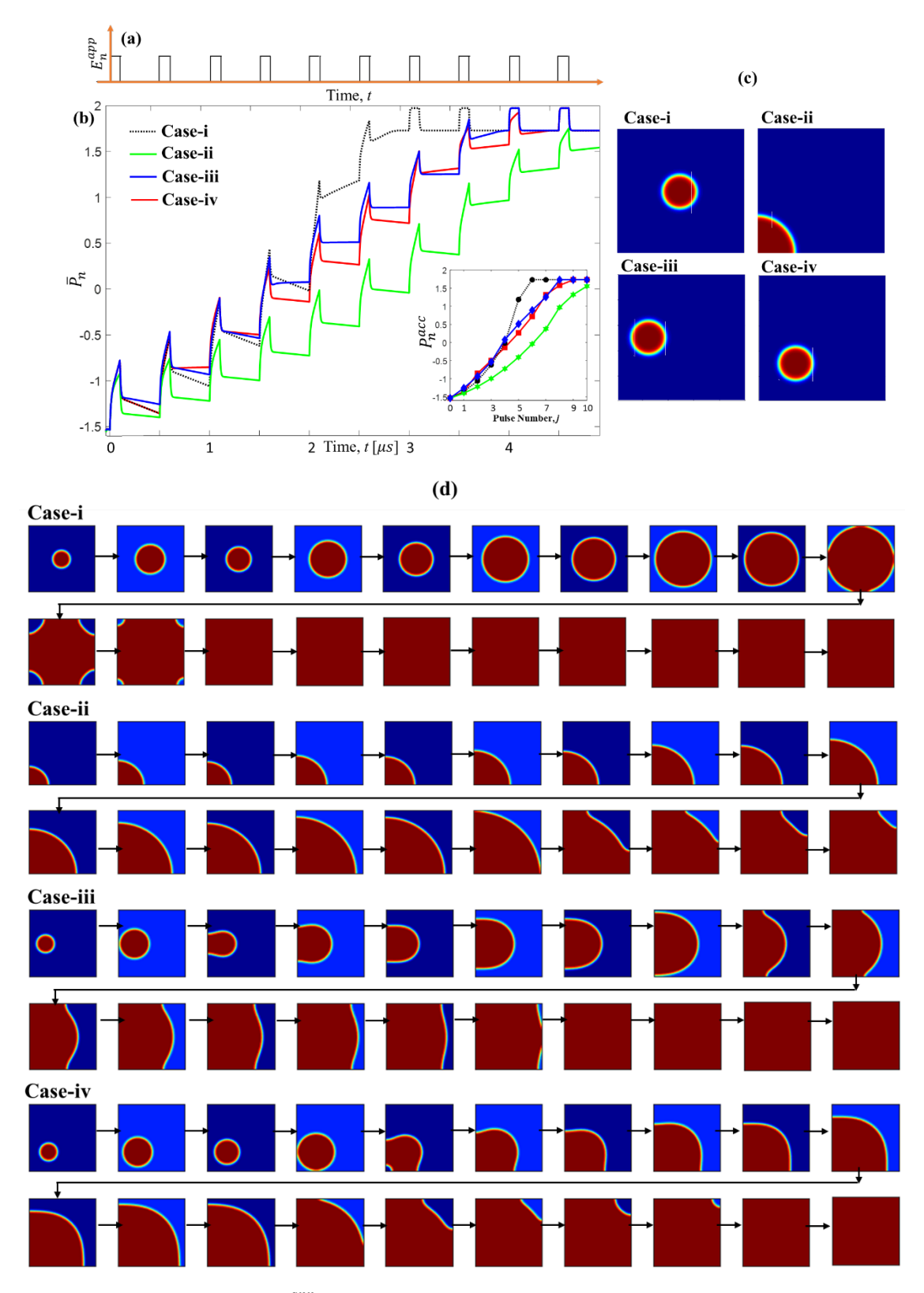


**Fig. S5:** (a) Applied E-field pulse sequences  $(E_{n,max}^{app} = 0.9, T_{on} = 100ns \text{ and } T_{off} = 400ns)$ . (b) Transient  $P_n$  and accumulated polarization  $(P_n^{acc}, \text{ at the inset})$  for different positions of pinned domain. (c) Initial P-map showing the position of pinned domain. (d) P-map at the end of each excitation and relaxation sequences (plotted sequentially) for all the considered cases.

#### **Spontaneous Relaxation:**

To start with, let us consider an FE grain, exhibiting a circularly nucleated domain (R1), as shown in Fig. S6. Note, that the domain holds a polar symmetry.

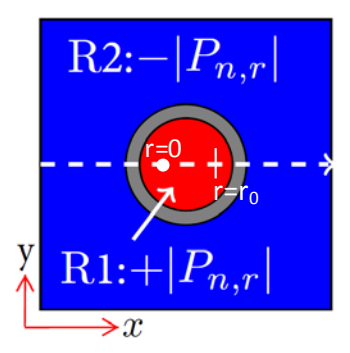


Fig. S6: 2D circular domain-wall (DW) separating two domain (R1 and R2)

Therefore, in polar coordinate, the term  $\nabla^2 P_n$  can be written as,

$$\nabla^2 P_n = \frac{\partial^2 P_n}{\partial r^2} + \frac{1}{r} \frac{\partial P_n}{\partial r} + \frac{1}{r^2} \frac{\partial^2 P_n}{\partial \theta^2}$$

Now, we can assume the center of the R1 domain as the center of the polar coordinate (r = 0). Also, due to polar symmetry, at a particular r,  $P_n(\theta)$  =constant and  $\frac{\partial^2 P_n}{\partial \theta^2}$  = 0. Therefore, we can write the equation as following.

$$\nabla^2 P_n = \frac{\partial^2 P_n}{\partial r^2} + \frac{1}{r} \frac{\partial P_n}{\partial r}$$

Now, let us assume  $P_n(r)$  is an odd symmetric function with a center of symmetry at r=r' (r=r' is the DW center). Therefore, we can immediately state that  $\frac{\partial P_n}{\partial r}$  will be even symmetric and  $\frac{\partial^2 P_n}{\partial r^2}$  will be odd symmetric with a center of symmetry at r=r'. However, the term  $\frac{1}{r}$  is only symmetric with respect to '0' (r=r' is not a symmetry point). Therefore, the second term in the above equation is asymmetric for any  $r' \neq 0$  and that leads to an asymmetric  $\nabla^2 P_n$ . To visualize different components of  $\nabla^2 P_n$ , we plot  $\frac{\partial^2 P_n}{\partial r^2}$ ,  $\frac{\partial P_n}{\partial r}$ , and  $\frac{\partial^2 P_n}{\partial r^2}$  with respect to r in the figure below (Fig. S7).

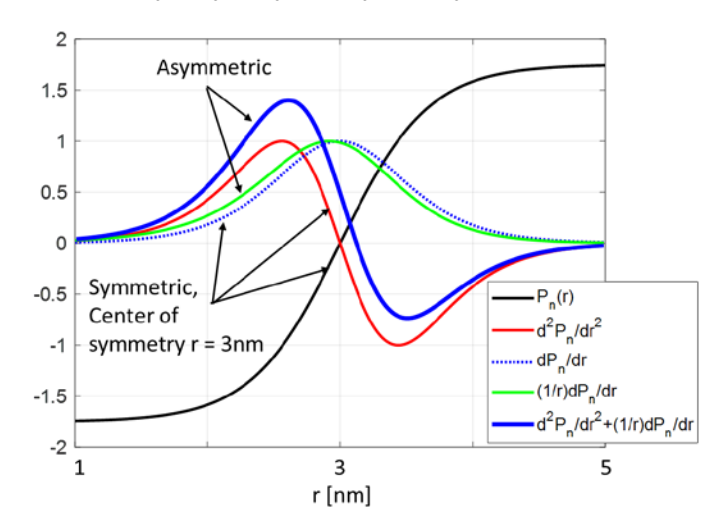


Fig. S7: Different components of  $\nabla^2 P_n$  with respect to  $P_n$ 

Note: \*\*Even if the second term is symmetric (not possible though), it is important to note that the summation of an odd symmetric and even symmetric function is always asymmetric.

As  $E_n^{int}$  becomes spatially asymmetric, where  $|E_n^{int}| > 1$  at the inner interface and  $|E_n^{int}| < 1$  at the outer interface of DW. Such asymmetry in the  $E_n^{int}$  causes the DW to undergo an effective inward force ( $\propto P \times E_n^{int}$ ). (Whereas, in case of 1D DW, such force was oppositely balanced due to symmetric nature of  $E_n^{int}$  distribution). Due to such inward force, the DW becomes unstable and R1 region shrinks spontaneously with time. Recall that the R1 domain corresponds to +P and R2 domain corresponds to -P. Therefore, Due to the spontaneous shrinking (decreasing in area) of R1 domain area, the average polarization of the grain  $(\overline{P}_n)$  decreases spontaneously and that leads to DW-instability driven polarization relaxation.

#### **Spontaneous Excitations:**

Each DW contains a spatial variation in polarization (-P to +P). Due to such polarization variation, each DW exhibits a local interaction field  $(E_n^{int} = K\nabla^2 P_n)$ . A typical plot of polarization distribution  $(P_n(x))$  and the corresponding  $E_n^{int}(x)$  is shown below (Fig. S8(a)). Note that,  $E_n^{int}(x) = 0$  at  $|x - x_0| \to \infty$ , where,  $x_0$  is the center of the domain wall. However, when two DW come sufficiently close (~less than a DW width) to each other, their interaction field overlaps with each other within the intermediate domain and hence, the total interaction field increases over the equilibrium value (shown in Fig. S8(b) and Fig S8(c)). Such increase in  $E_n^{int}$  from its equilibrium value induces spontaneous P-switching (-P to +P) in R2 domain and that leads to spontaneous P-excitation component.

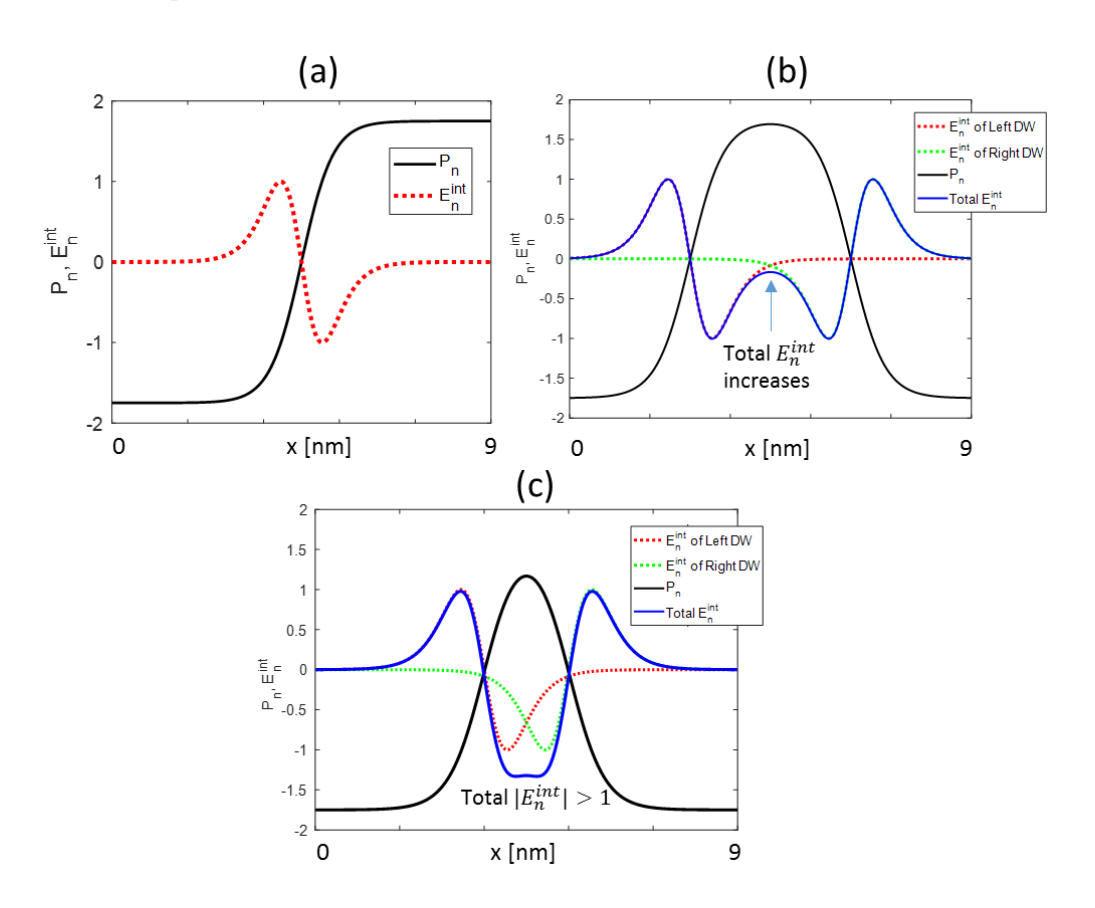


Fig. S8: (a)  $E_n^{int}$  for a standalone DW, (b)  $E_n^{int}$  for two DWs with a distance less than the DW width, (c)  $E_n^{int}$  for two DWs with a distance much less than the DW width.

#### Differences in P-switching dynamics between case-1 (homogeneous $E_C$ ) and case-2 (non-homogeneous $E_C$ )

In the main text, we discuss the P-switching dynamics in an FE grain by considering two cases. In case-1, we considering homogeneous  $E_C$ , where the creation of the DW is pre-conditioned with the assumption of a pinned domain. On the other hand, in case-2, we consider a local distribution of  $E_C$  in an FE grain, where the creation of the DW depends on the initial nucleation of low  $E_C$  regions (near the grain edges). In both the cases, we observe spontaneous relaxation in the absence of an applied Efield that originates from DW instability. In case-1, the DW instability occurs due to the asymmetry in  $E_n^{int}$ , which is the outcome of 2D nature of the DW. However, in case-2, such asymmetry in  $E_n^{int}$  gets enhanced due to non-homogeneity in  $E_C$  ( $E_C$  of the switched domains are lower compared to the  $E_C$  of the domains those are not switched yet). Therefore, the spontaneous P-relaxation is higher in case-2 compared to case-1.

Also, we discuss the spontaneous excitation of polarization for both the cases. In case-1, spontaneous *P*-excitation takes place due to the DW instability near the grain edge. In contrast, in case-2, spontaneous *P*-excitation occurs due to the interaction between two DWs that makes the intermediate region (between the DWs) unstable, thus, spontaneously switching to +*P*. It is important to note that the area of the domain that undergoes spontaneous *P*-excitation is less in case-1 (regions near the grain edges, Fig. 3(b)) compared to case-2 (regions in between the DWs, Fig. 4(d)). Therefore, the spontaneous *P*-excitation is more prominent in case-2 compared to case-1.

#### Extraction of $E_C$ distribution from experiment:

An FE sample exhibits an ensemble of grains (due to polycrystallinity) with different geometries and areas. As the mean coercive field  $(E_C)$  of a grain depends on its size [5], therefore, the FE film manifest a spatial distribution of  $E_C$ . Due to such  $E_C$  distribution among the grains, for a given maximum applied E-field  $(E_{max})$ , a certain number of grains (with  $E_C < E_{max}$ ) undergo polarization switching, giving rise to a remnant polarization  $(P_R)$ . With the increase in  $E_{max}$ , increased number of grains undergo polarization switching leading to an increase in  $P_R$ . Let us assume,  $P_R = P_{RI}$  for  $E_{max} = E_{maxI}$  and  $P_R = P_{R2}$  for  $E_{max} = E_{max2} = E_{maxI} + \Delta E$ , where  $\Delta E$  is small positive increase in  $E_{max}$  (i.e.  $E_{max} \ge E_{maxI}$ ). Therefore, the increase in  $P_R$  ( $\Delta P_R = P_{R2} - P_{RI}$ ) is proportional to the **area of newly switched grains**. Also, the mean coercive field of those newly switched grains must be  $E_{max}$ . Note that, for a sufficiently high  $E_{max}$ , it is possible to switch all the grains and that provides the highest  $P_R \approx P_{R,max}$  (in principle, further increase in  $E_{max}$  should not provide a significant increase in  $E_R$ ). Putting this all together,  $E_R = E_{max}$  represents the % area of the sample (or area fraction) for which  $E_C \approx E_{max2}$ .

To experimentally extract such  $E_C$  distribution, we measure the P-E loop of HZO for different sweep ranges of the applied field (i.e. for different  $E_{max}$ ) (Fig. S9(a)). Corresponding remnant polarization ( $P_R$ ) versus  $E_{max}$  is shown in Fig. S9(b). Then we calculate the increase in  $P_R(\Delta P_R)$  for the each  $E_{max}$  Finally, we calculate the area fraction corresponding to an  $E_C$  by normalizing  $\Delta P_R$  (at  $E_{max}$ = $E_C$ ) with respect to the maximum  $P_R(P_{R,max}$ -Fig. S5(b))The resultant  $E_C$  distribution is shown in Fig. S9(c).

$$\% Area @ E_c = \frac{\Delta P_R}{P_{R,max}}$$

$$(a)$$

$$(b)$$

$$(c)$$

$$(b)$$

$$(c)$$

$$(c)$$

$$(d)$$

$$(d)$$

$$(d)$$

$$(e)$$

$$(d)$$

$$(e)$$

$$(e)$$

$$(e)$$

$$(e)$$

$$(e)$$

$$(e)$$

$$(f)$$

**Fig. S9:** (a) Measured P-E characteristics of HZO for different maximum value of applied E-field. (b) Remnant polarization ( $P_R$ ) for different maximum value of applied E-field. (c) Extracted global  $E_C$  distribution in HZO (red) and corresponding Gaussian fit (dashed black) with mean = 1.1, standard deviation = 0.175.

#### Inclusion of the coupling terms between the strain/stress and the polarization:

Under TDGL formalism, the polarization state equation for  $P_z$  can be written as [7],

$$-\rho \frac{\partial P_z}{\partial t} = \left[2\alpha_1 - (2Q_{11}\sigma_3 + 2Q_{12}(\sigma_1 + \sigma_2))\right]P_z + 4\alpha_{11}P_z^3 + 6\alpha_{111}P_z^5 + 2\alpha_{12}P_z(P_x^2 + P_y^2) + \alpha_{112}\left(4P_z^3(P_y^2 + P_x^2) + 2P_z(P_x^4 + P_y^4)\right) - Q_{44}(\sigma_{12}P_x + \sigma_{13}P_y) - g_{44}\left[\frac{\partial^2 P_z}{\partial x^2} + \frac{\partial^2 P_z}{\partial y^2}\right] - E_z^{app}$$

Here, we use Voigt's notation for the coefficients. So,  $1 \equiv x$ ,  $2 \equiv y$ ,  $3 \equiv z$ . Q = electrostriction coefficient, g = gradient energy coefficient and  $\sigma =$  stress.

Now, based on the assumption of  $P_x = P_y = 0$ , we can re-write the equation as,

$$-\frac{\partial P_z}{\partial t} = \left[2\alpha_1 - (2Q_{11}\sigma_3 + 2Q_{12}(\sigma_1 + \sigma_2))\right]P_z + 4\alpha_{11}P_z^3 + 6\alpha_{111}P_z^5 - g_{44}\left[\frac{\partial^2 P_z}{\partial x^2} + \frac{\partial^2 P_z}{\partial y^2}\right] - E_z^{app}$$

Now,  $\sigma_1$ ,  $\sigma_2$  and  $\sigma_3$  can be written as

$$\sigma_{1} = \sigma_{2} = (s_{11}U_{2} - s_{12}U_{3})/(s_{11}^{2} - s_{12}^{2})$$

$$\sigma_{3} = (s_{11}U_{3} - s_{12}U_{2})/(s_{11}^{2} - s_{12}^{2})$$

$$U_{3} = Q_{11}[(P_{Z}^{S})^{2} - (P_{Z})^{2}]$$

$$U_{2} = Q_{12}[(P_{Z}^{S})^{2} - (P_{Z})^{2}]$$

Here,

Where,  $P_Z^S$  is spontaneous polarization along z-axis.

Now, we can write,

$$\sigma_{2} = \frac{s_{11}U_{3} - s_{12}U_{2}}{s_{11}^{2} - s_{12}^{2}} = \frac{s_{11}Q_{11}[(P_{Z}^{S})^{2} - (P_{Z})^{2}] - s_{12}Q_{12}[(P_{Z}^{S})^{2} - (P_{Z})^{2}]}{s_{11}^{2} - s_{12}^{2}}$$

$$\sigma_{3} = \frac{s_{11}U_{2} - s_{12}U_{3}}{s_{11}^{2} - s_{12}^{2}} = \frac{s_{11}Q_{12}[(P_{Z}^{S})^{2} - (P_{Z})^{2}] - s_{12}Q_{11}[(P_{Z}^{S})^{2} - (P_{Z})^{2}]}{s_{11}^{2} - s_{12}^{2}}$$

Thus one can obtain,

$$\begin{split} &-\frac{\partial P_{z}}{\partial t} = \left[2\alpha_{1} - \left(2Q_{11}\frac{s_{11}Q_{12}\left[\left(P_{Z}^{S}\right)^{2} - \left(P_{Z}\right)^{2}\right] - s_{12}Q_{11}\left[\left(P_{Z}^{S}\right)^{2} - \left(P_{Z}\right)^{2}\right]}{s_{11}^{2} - s_{12}^{2}}\right.\\ &+ 4Q_{12}\frac{s_{11}Q_{11}\left[\left(P_{Z}^{S}\right)^{2} - \left(P_{Z}\right)^{2}\right] - s_{12}Q_{12}\left[\left(P_{Z}^{S}\right)^{2} - \left(P_{Z}\right)^{2}\right]}{s_{11}^{2} - s_{12}^{2}}\right)\right]P_{z} + 4\alpha_{11}P_{z}^{3} + 6\alpha_{111}P_{z}^{5}\\ &- g_{44}\left[\frac{\partial^{2}P_{z}}{\partial x^{2}} + \frac{\partial^{2}P_{z}}{\partial y^{2}}\right] - E_{z}^{app} \end{split}$$

$$\begin{split} -\frac{\partial P_z}{\partial t} &= \left[2\alpha_1 - \left(2Q_{11}\frac{s_{11}Q_{12} - s_{12}Q_{11}}{s_{11}^2 - s_{12}^2} + 4Q_{12}\frac{s_{11}Q_{11} - s_{12}Q_{12}}{s_{11}^2 - s_{12}^2}\right) \left[(P_Z^S)^2 - (P_Z)^2\right]\right] P_z + 4\alpha_{11}P_z^3 + 6\alpha_{111}P_z^5 \\ &- g_{44}\left[\frac{\partial^2 P_z}{\partial x^2} + \frac{\partial^2 P_z}{\partial y^2}\right] - E_z^{app} \end{split}$$

Let us define 
$$\eta = 2Q_{11} \frac{s_{11}Q_{12} - s_{12}Q_{11}}{s_{11}^2 - s_{12}^2} + 4Q_{12} \frac{s_{11}Q_{11} - s_{12}Q_{12}}{s_{11}^2 - s_{12}^2}$$

Note that the polarization-strain coupling provides a liner and a quadratic terms of polarization. Therefore, we can write.

$$-\frac{\partial P_z}{\partial t} = \left[2\alpha_1 - (P_z^S)^2 \eta\right] P_z + \left[4\alpha_{11} + \eta\right] P_z^3 + 6\alpha_{111} P_z^5 - g_{44} \left[\frac{\partial^2 P_z}{\partial x^2} + \frac{\partial^2 P_z}{\partial y^2}\right] - E_z^{app}$$

We can re-write the equation as,

$$-\frac{\partial P_z}{\partial t} = \alpha P_z + \beta P_z^3 + \gamma P_z^5 - K \left[ \frac{\partial^2 P_z}{\partial x^2} + \frac{\partial^2 P_z}{\partial y^2} \right] - E_z^{app}$$
 (S20)

Where,

$$\alpha = 2\alpha_1 - (P_Z^S)^2 \eta$$
$$\beta = 4\alpha_{11} + \eta$$
$$\gamma = 6\alpha_{111}$$
$$K = q_{44}$$

Note that the similar approach has also been presented in [8,9]. It is important to note that, such effective representation of state equation by merging the contribution of strain-polarization coupling with the free energy coefficient is possible because of the assumption of  $P_x = P_y = 0$ . However, in presence of this in-plane polarization component (provided that o-phase c-axis is parallel to in-plane), a self-consistent simulation between the state equations of polarization and strain/stress is required.

It is important to mention that the values of  $\alpha_1$ ,  $\alpha_{11}$ ,  $\alpha_{111}$ ,  $Q_{33}$  is not well-defined in literature. However, we use equation (S20) to calibrate the experimentally measured polarization versus electric field characteristics to calculate the  $\alpha$ ,  $\beta$  and  $\gamma$  values in normalized unit. We have discussed the calibration of  $\alpha$ ,  $\beta$  and  $\gamma$  values (in normalized space) at the beginning of this supplementary document.

#### **References:**

- [1] K. M. Rabe, C. H. Ahn, and J.-M. Triscone, *Physics of Ferroelectrics A Modern Perspective* (Springer, 2007).
- [2] S. Nambu and D. A. Sagala, Phys. Rev. B, 50, 5838 (1994).
- [3] F. Xue, et al., Acta Materialia, Vol. 61, no. 8, pp 2909-2918, 2013.
- [4] L. Q. Chen and W. Yang, Phys. Rev. B, 50, 15752.
- [5] J. S. Liu, S. R. Zhang, H. Z. Zeng, C. T. Yang, and Y. Yuan, *Phys. Rev. B*, 72, 172101.
- [6] Eugene A. Eliseev, et. al., Phys. Rev. B 85, 045312 (2012).
- [7] Eugene A. Eliseev, Anna N. Morozovska, George S. Svechnikov, Peter Maksymovych, and Sergei V. Kalinin, Phys. Rev. B 85, 045312 (2012).

- [8] Qingping Meng, Myung-Geun Han, Jing Tao, Guangyong Xu, David O. Welch, and Yimei Zhu, Phys. Rev. B 91, 054104 (2015)
- [9] Yijia Gu, Menglei Li, Anna N. Morozovska, Yi Wang, Eugene A. Eliseev, Venkatraman Gopalan, and Long-Qing Chen, Phys. Rev. B 89, 174111 (2014)